Molecular Crystallization Controlled by pH Regulates Mesoscopic Membrane Morphology

Cheuk-Yui Leung,[†,#] Liam C. Palmer,[‡,#] Bao Fu Qiao,[§,#] Sumit Kewalramani,[§] Rastko Sknepnek,[§] Christina J. Newcomb,[§] Megan A. Greenfield,[⊥] Graziano Vernizzi,[§,∥] Samuel I. Stupp,[‡,§,¶] Michael J. Bedzyk,[†,§] and Monica Olvera de la Cruz[‡,§,⊥,*]

[†]Physics and Astronomy, [‡]Department of Chemistry, [§]Materials Science and Engineering, and [⊥]Chemical and Biological Engineering, Northwestern University, Evanston, Illinois 60208, United States, [∥]Department of Physics, Siena College, Loudonville, New York 12211, United States, and [¶]Department of Medicine and Institute for BioNanotechnology in Medicine, Northwestern University, Chicago, Illinois 60611, United States

ABSTRACT Coassembled molecular structures are known to exhibit a large variety of geometries and morphologies. A grand challenge of self-assembly design is to find techniques to control the crystal symmetries and overall morphologies of multicomponent systems. By mixing +3 and −1 ionic amphiphiles, we assemble crystalline ionic bilayers in a large variety of geometries that resemble polyhedral cellular crystalline shells and archaea wall envelopes. We combine TEM with SAXS and WAXS to characterize the coassembled structures from the mesoscopic to nanometer scale. The degree of ionization of the amphiphiles and their intermolecular electrostatic interactions are controlled by varying pH. At low and high pH values, we observe closed, faceted vesicles with two-dimensional hexagonal molecular arrangements, and at intermediate pH, we observe ribbons with rectangular-C packing. Furthermore, as pH increases, we observe interdigitation of the bilayer leaflets. Accurate atomistic molecular dynamics simulations explain the pH-dependent bilayer thickness changes and also reveal bilayers of hexagonally packed tails at low pH, where only a small fraction of anionic headgroups is charged. Coarse-grained simulations show that the mesoscale geometries at low pH are faceted vesicles where liquid-like edges separate flat crystalline domains. Our simulations indicate that the curved-to-polyhedral shape transition can be controlled by tuning the tail density in regions where sharp bends can form the polyhedral edges. In particular, the pH acts to control the overall morphology of the ionic bilayers by changing the local crystalline order of the amphiphile tails.

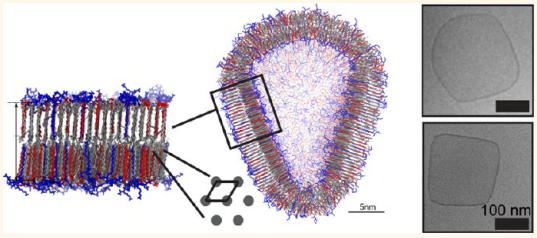

KEYWORDS: atomistic simulations · membrane morphology · pH · self-assembly · electrostatics · X-ray scattering

A large variety of amphiphilic molecules with charged headgroups self-assemble into closed structures akin to cell membranes.[1−4] Many closed membranes including viral capsids,[5] halophilic organism envelopes,[6,7] and bacterial microcompartments[8−10] spontaneously adopt complex shapes, including icosahedra and other polyhedral geometries, which suggests that these envelopes are likely to exhibit internal crystalline ordering within their membranes. The ability to fabricate nanocontainers with specific internal structures and geometries[11] is highly desirable for applications including catalysis, gene therapy, and targeted drug delivery.[12−14] Specifically, nanoswitches that can convert chemical energy into mechanical energy could be used to open and close membranes or to create large structural changes in the membrane thickness. However, it remains unknown how the specific crystal structure within a membrane affects its overall morphology on multiple length scales. Nevertheless, such a mechanism must exist as shown by many natural systems; for instance, the robust envelope of halophilic microorganisms, which allows them to survive in extreme environments, takes a square geometry,[6] even though the cell wall is actually composed of a hexagonal lattice[7] of various lipids.

In the present work, we explore the possibility of using electrostatic interactions as one parameter to drive structural changes in the coassemblies of ionic amphiphiles into lattices that are expected to form nanocontainers with specific shape and composition.[15−18] Specifically, we show that the pH

* Address correspondence to m-olvera@northwestern.edu.

Received for review September 18, 2012 and accepted November 27, 2012.

Published online November 27, 2012
10.1021/nn304321w

of the solution can be used to vary the equilibrium shape of ionic crystalline amphiphile membranes, *via* a fascinating multiscale process that correlates global mesoscopic shape to the local nanoscale crystalline structure. Ionic coassemblies generally disassemble at physiological salt concentrations.[19−22] Therefore, we use long alkyl tail amphiphiles for which the additional intertail van der Waals attractions lead to salt-stable, ionically driven coassemblies.

While single-tailed ionic amphiphiles typically form micelles,[23] mixtures of oppositely charged amphiphiles have a distinct behavior resulting in bilayers that can even self-assemble into micrometer-sized icosahedral vesicles under salt-free conditions.[16,24] Previous work on polymerizable amphiphiles[17] showed that a large charge imbalance between the cationic and anionic headgroups enables their coassembly into nanoscale faceted structures.[25] By coassembling oppositely charged surfactants without a polymerizable group, we demonstrate that electrostatics provides the essential "glue" for the crystallization of the tails and the potential to modify the structure by changing the solution pH. In fact, the solution pH controls electrostatic correlations, which in turn determine the two-dimensional crystalline structure. Furthermore, crystalline domains can lead to the formation of closed shell shapes other than the ubiquitous icosahedra. Those shapes, which resemble organelle microcompartments[10] and faceted halophilic organisms,[6] are stable over time even at high salt concentrations. To observe structural changes at the mesoscopic and the atomistic length scales, we use transmission electron microscopy (TEM) for the 10 to 1000 nm length scale (overall membrane morphology), *in situ* small-angle X-ray scattering (SAXS) for observing the 1−100 nm length scale (membrane wall thickness), and *in situ* wide-angle X-ray scattering (WAXS) to observe the angstrom scale (two-dimensional molecular crystal structure within the membrane).

RESULTS AND DISCUSSION

Figure 1a depicts the two oppositely charged amphiphiles used in this study, with dissimilar headgroups but identical hydrophobic tails. Amphiphile C_{15}-COOH is a monovalent anionic fatty acid (palmitic acid). Amphiphile C_{16}-K_3 comprises a trivalent cationic headgroup of three lysine (K) amino acids and a hydrophobic palmitoyl tail.[26] The charge ratio of +3/−1 (rather than +1/−1)[16] is expected to reinforce the ionic correlations and maximize the packing of the hydrophobic tails into crystalline lattices. Cryogenic TEM (Figure 1b−d) and quick-freeze/deep-etch TEM (see Supporting Information, Figure S1) are used to image the hydrated structures. As expected for simple surfactants with a large headgroup, cation C_{16}-K_3 dissolves in water and forms micelles of ∼10 nm diameter (Figure S1). It can be coassembled with water-insoluble

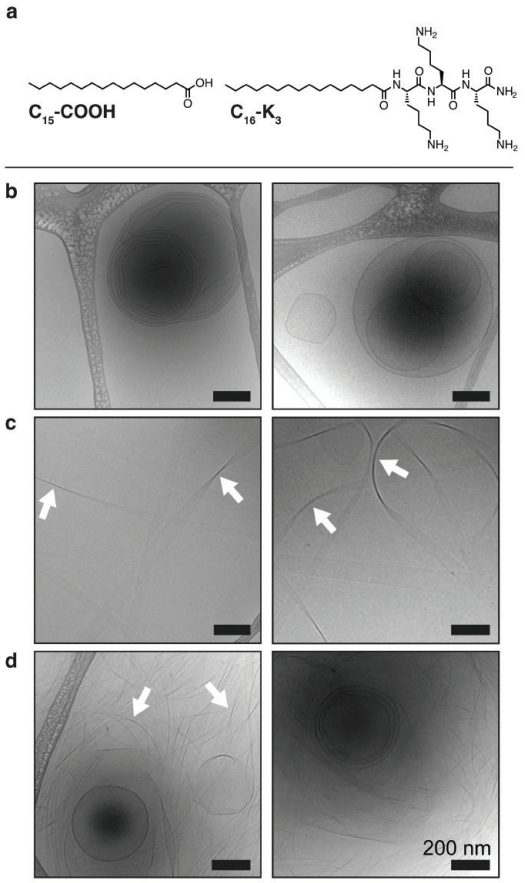

Figure 1. Coassembly of oppositely charged amphiphiles shows vesicles in aqueous solution. (a) Charged amphiphiles used for ionic coassembly: −1 palmitic acid (C_{15}-COOH) with +3 trilysine (C_{16}-K_3). Representative cryogenic TEM images of structures formed from a mixture of C_{15}-COOH and C_{16}-K_3 in water. (b) At pH 5, only vesicles are observed. (c) Solutions at pH 8 show flat ribbons (indicated by white arrows). (d) At pH 10, the sample shows a mixture of vesicles and ribbons.

palmitic acid C_{15}-COOH at different pH values to control the shape of membranes, as shown in Figure 1b−d. The cation/anion mixture images show a pH-dependent diversity of shapes including closed unilamellar and multilamellar faceted vesicles (Figure 1b,d) and open sheets or ribbons (Figure 1c,d). All of these structures are consistent with a bilayer membrane morphology as discussed below.

Simultaneously collected SAXS and WAXS data provide *in situ* information on the nanoscale morphology and atomic length-scale crystallinity, respectively. The processed SAXS−WAXS data are shown in Figure 2a as a function of the scattering vector $q = 4\pi \sin\theta/\lambda$. For pH 4, 8, and 10, the SAXS intensity in the Porod region ($q < 0.3$ nm^{-1}) decreases as $\sim q^{-2}$, indicating scattering from two-dimensional structures.[27] We note that a collection of three-dimensional objects would cause a $\sim q^{-4}$ decrease and one-dimensional fibers would show a q^{-1} decrease. These observations imply that the structures observed in TEM are composed of two-dimensional bilayers. The features in the scattering

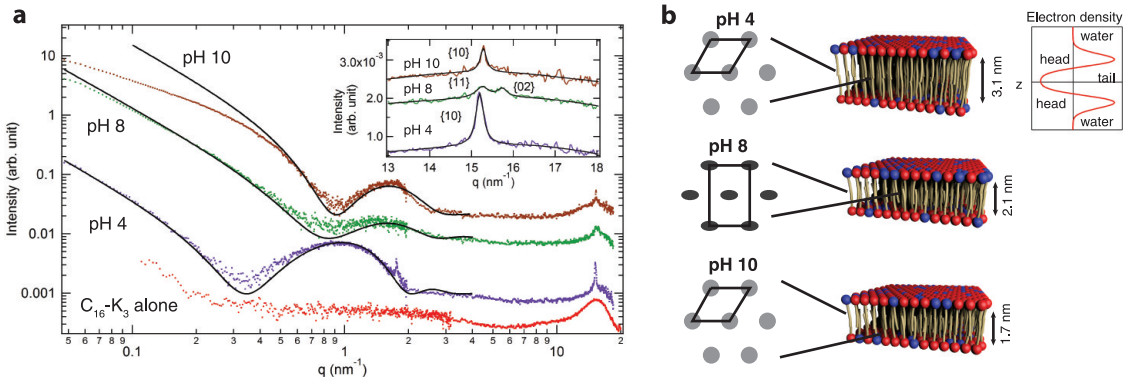

Figure 2. X-ray scattering from bilayers in solutions. (a) *In situ* small- and wide-angle X-ray scattering data showing the background-subtracted scattered intensity *versus* the scattering vector q for cation C_{16}-K_3 alone (bottom) and mixtures of acid C_{15}-COOH and cation C_{16}-K_3 as the pH is increased from 4 to 10. The data sets are offset vertically for clarity. The black lines are the fits over the range $0.05 < q < 4$ nm^{-1}. Deviations in the fits are likely due to sample polydispersity. Inset: WAXS data and peak fits of the mixed cation/anion samples mixed samples indicate formation of crystalline lattices. (b) Schematic representations for the bilayer model at pH 4, 8, and 10 fitted to a bilayer model. Changes are observed in the thickness of the hydrophobic portion of the bilayer and the packing of the alkyl tails (green rectangles) into either an orientationally disordered hexagonal or a rectangular-C lattice. Vertical distortion is exaggerated in the rectangular-C model for clarity.

TABLE 1. Lattice Parameters and Membrane Thicknesses Obtained From X-ray Scattering and Atomistic MD Simulation

	2D crystal lattice	domain size (nm)	lattice constant (nm)	area per molecule (nm^2)		membrane thickness (nm)		hydrophobic thickness (nm)	
pH	WAXS	WAXS	WAXS	WAXS	atomistic simulation	SAXS	atomistic simulation	SAXS	atomistic simulation
3	hexagonal	31	$a = 0.477$	0.197		5.3		3.1	
4	hexagonal	29	$a = 0.477$	0.197	0.2	5.3	4.9	3.1	3.6
7	hexagonal	20	$a = 0.474$	0.195		4.2		2.4	
8	rectangular-C	21	$a = 0.479$	0.192	0.2	4.1	3.9	2.1	2.1
			$b = 0.800$						
10	hexagonal	35	$a = 0.474$	0.195		4.3		1.7	

pattern that would sense the 200−500 nm size of the vesicles occur below our 0.05 nm^{-1} cutoff range in q, so it is important to complement these SAXS measurements with the TEM images. Fitting the SAXS data to a bilayer model, as shown in Figure 2b, gives the thickness information for each membrane (Table 1). We estimate that the thicknesses of the hydrophobic tail regions are *ca.* 3.1 nm for pH 3−7 and *ca.* 2.1 nm for pH >7, as shown in Figure 2b. For pH 4, the hydrophobic thickness of 3.1 nm is slightly shorter than the length expected for two C_{16} alkyl tails in their fully extended conformation (∼3.8 nm), whereas at pH 8, the thickness is consistent with the length of one C_{16} alkyl tail (∼1.9 nm), as expected for a more highly interdigitated bilayer.

The comparison of the WAXS data for the catanionic mixtures to the data for the pure cation (Figure 2a) shows that the ordered packing of lipid tails arises only in structures formed due to electrostatic interactions between the oppositely charged amphiphiles. The WAXS data for the solution of cation alone (red dots in Figure 2a) do not show diffraction peaks, as expected for a disordered micelle. By contrast, diffraction peaks appear in the WAXS region for the catanionic mixtures. For pH <7 and pH >10, the appearance of a single diffraction peak indicates that the molecules are packed in a two-dimensional hexagonal lattice, whereas the presence of two diffraction peaks for pH 8−9 indicates a rectangular-C structure. The lattice parameters and packing densities as a function of pH are listed in Table 1. Interestingly, very similar vesicle shapes are observed by TEM at pH 5 and 10 (Figure 1b,d), while high aspect ratio nanoribbons are abundant at pH 8 (Figure 1c).

The hexagonal−rectangular−hexagonal transition as pH increases, illustrated in Figure 2b, can be explained by the enhanced electrostatic attractions between the cationic and anionic molecules in the pH 8−9 regime, where both the palmitic acid headgroups ($pK_a \sim 7.5$) and the trilysine cationic molecules ($pK_a \sim 10.5$) are expected to be nearly fully charged. In the low pH regime, the cations are fully charged and the degree of ionization of the anion is very low, while the reverse is true at high pH. This will be discussed below in conjunction with Figure 3e. The WAXS-derived area per tail (A_t = 0.192 nm^2) for pH 8−9 is less than the observed $A_t = 0.197$ nm^2 for pH 3−7 and $A_t = 0.195$ nm^2 for pH ≥ 10, which corresponds to the maximum packing density of the orientationally disordered (cylindrical) alkyl tails on a hexagonal lattice.[28] Therefore, a reduction in A_t

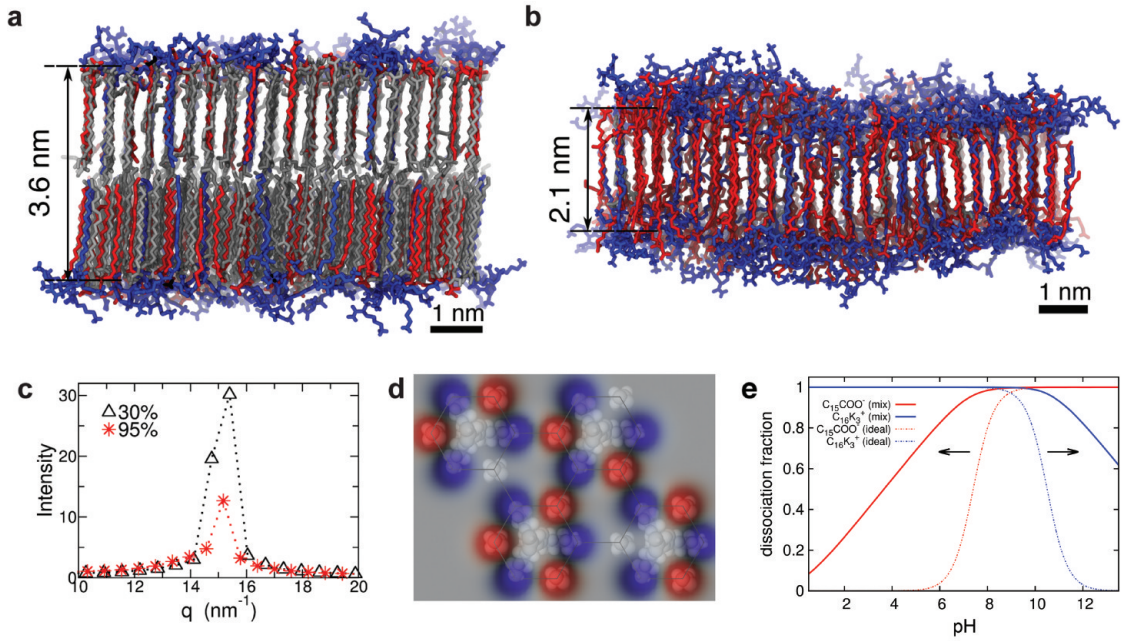

Figure 3. Atomistic MD simulation of bilayers. (a,b) Snapshots of the typical bilayer configuration from the explicit solvent with (a) 30% and (b) 95% average degree of ionization of the anionic molecules. The cationic, anionic, and neutral anionic molecules are shown in blue, red, and gray, respectively. Solvent (water) molecules are omitted for clarity. The hydrophobic thicknesses of the membranes are presented. (c) Calculated scattering structure factor, which is comparable to the WAXS data in Figure 2. (d) Cartoon of the amphiphile headgroups assumed to be projected into a two-dimensional hexagonal lattice formed by the amphiphile tails (not to scale). The heads of the amphiphiles are at the vertices of the hexagonal lattice and can be neutral (gray) or charged *via* dissociation with charge −1 (red) for the palmitic acid and +1 (blue) for the lysine groups; every three nearest-neighbor lysine side chains are connected *via* a common tail to form the trilysines. (e) Fraction of dissociated trilysine (blue curves) and palmitic (red curves) sites as a function of pH obtained by Monte Carlo simulation assuming the lattice shown in (d) for the distribution of cationic (+3) and anionic (−1) headgroups for 94 mM monovalent salt concentration. We show for reference the degree of dissociation for the ideal situation of isolated headgroups in the bulk (dashed lines). When mixed in a lattice, their dissociating is enhanced. All curves are generated assuming pK_a(COOH) = 7.4 and pK_a(NH^{3+}) = 10.5. The dissociation is sensitive to the variations in pK_a of lysine headgroups, which we know is lower when the three heads are connected and confined to the surface; when pK_a(NH^{3+}) = 7.5, for example, the 100% dissociation of both groups is not reached at any pH value (see Supporting Information).

necessarily requires an orientational ordering of the backbone plane of the alkyl tails and a distortion of the hexagonal lattice, which in this case leads to a rectangular-C lattice (Figure 2b). The sum of integrated WAXS peak intensities, which is a measure of the degree of crystallization, is lower at pH 8 than at pH 4. Therefore, bilayers containing anionic molecules with a higher degree of ionization are less crystalline than bilayers with a lower fraction of ionized groups (*i.e.*, the degree of ionization inversely affects the degree of crystallinity). While these experimental results clearly demonstrate structural changes at the nanoscale and mesoscale, they are not sufficient to identify the detailed mechanism and the behavior of the system at the level of individual molecules.

As indicated above, the X-ray experiments reveal that the membrane thickness can be controlled by adjusting the pH of the solution. To explore the mechanism of such change, molecular dynamics (MD) simulations are performed at both atomistic and molecular resolution. Specifically, we simulate systems with a low degree of ionization of the palmitic acid groups to mimic the low-pH data and a high degree of ionization to explain the intermediate-pH data. Moreover, to reveal the structures of the faceted vesicles experimentally observed at low pH, coarse-grained MD simulations are performed at the molecular resolution. That is, a series of simulations are performed to reveal the morphological transformations across length scales and the origin of the observed shell geometries.

We first describe the atomistic simulations performed to describe the pH-induced bilayer thickness changes. The snapshots from long-time scale (up to 1 μs) atomistic molecular dynamics simulations show electroneutral systems with 30% (Figure 3a) and 95% (Figure 3b) average ionization of the palmitic acid molecules, which correspond roughly to pH 4 and 8, respectively. The bilayer structure is observed in both cases. Moreover, interdigitation between layers is observed only in systems with 95% ionization of the palmitic acid. Crystallization of the hydrocarbon tails is observed in both systems, as illustrated in Figure 3a,b. This is further supported by the diffraction peaks in the scattering structure factor of the hydrocarbon tails (Figure 3c), which is obtained from the Fourier transform of the corresponding radial distribution function (Figure S6 in Supporting Information). (Moreover, to provide evidence for the crystalline structures in the upper layer and in the lower layer, a movie showing

the rotation of the 30% system is provided in Supporting Information.) The positions of the peaks in Fourier transform (Figure 3c) agree well with those observed in the WAXS data at pH 4 and 8, respectively (Figure 2a). Furthermore, the scattering structure factors in Figure 3c suggest a relatively weaker degree of crystallization at 95% ionization of acid C_{15}-COOH, which is consistent with the smaller integrated intensity at pH 8 in WAXS. This difference in crystallinity indicates that a subtle balance among ionic correlations (which, as explained below, generate net attractions), van der Waals interactions, and chemical acid−base equilibria determines the crystalline structure. The area per tail is found to be ~0.2 nm^2 in both the 30 and 95% systems, which is consistent with the WAXS data (Table 1). The rectangular-C packing of the hydrocarbon chains was not reproduced by our atomistic MD simulations, which may be due to the limited length scale (<10.5 nm) and time scale (1 μs) of the simulation. Another reason may be attributed to the force field, which was not parametrized for crystalline phases, where the configuration entropy likely plays a more significant role than in the liquid phase. Monte Carlo simulations show how the pH is related to the degree of ionization of the molecules (Figure 3d). When the cationic and anionic amphiphiles coassemble (Figure 3e), the dissociation is more favorable when compared to the cases of isolated anionic and cationic molecules in solutions.[29,30] Therefore, headgroups are charged over a broad range of pH values. Removing salt enhances this effect (cf. Supporting Information).

Also indicated in Figure 3a,b are the MD-derived thicknesses of the hydrophobic tail regions of the membranes, which are found to be 3.6 nm for the 30% ionization system and 2.1 nm for the 95% ionization system and are consistent with the corresponding SAXS data in Figure 2b. The change of the bilayer thickness can be interpreted based on the imbalance between the excluded volume of the large cationic headgroups and the relatively small cross section of the hydrophobic tails, which is compensated by the relatively high proportion of uncharged palmitic acid C_{15}-COOH at low pH. When the pH is elevated, the imbalance between the excluded volumes of the headgroups and tails increases because there are not enough uncharged palmitic acid molecules to fill the voids. This imbalance is energetically unfavorable and can be compensated by the interdigitation of the hydrophobic tails in the upper and the lower leaflets, as illustrated in Figure 4, to maintain the attractive hydrophobic interactions (Table S1 in Supporting Information).

A simple estimate of the electrostatic correlations can explain the formation of the crystalline lattices on the vesicles. The electrostatic correlations are quantified by $l_B = e^2/4\pi\varepsilon_0\varepsilon_r k_B T$, the length at which the electrostatic interaction is comparable with the thermal

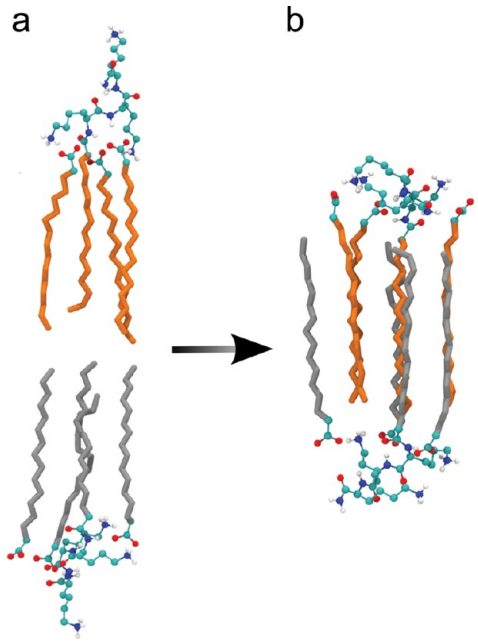

Figure 4. Bilayer structure (a) before (simulation time of 0 ns) and (b) after (1 μs) the interdigitation of the upper leaflet (hydrocarbons in orange) and the lower leaflet (hydrocarbons in silver) in the 95% system. Only a small fraction of the system is displayed for clarity. The process of the interdigitation is predominately induced by an increase of the hydrophobic interaction ($\Delta E = E_{after} - E_{before} = -3.56\ k_BT/nm^3$) relative to the ionic correlation between the opposite layers ($-1.38\ k_BT/nm^3$) (Table S1).

energy k_BT (where e is the unit charge, ε_r is the relative permittivity of the medium, and ε_0 is the dielectric permittivity of vacuum). The hydrocarbon tails are nonpolar with $\varepsilon_r \approx 1$, while $\varepsilon_r \approx 80$ in water. Consequently, the headgroups located between polar water and nonpolar tails experience a weaker dielectric response (typically the mean ε_r between the two media, *i.e.*, $\varepsilon_r \approx 40$), resulting in $l_B \approx 1.4$ nm, which is approximately three times the interchain distance observed by WAXS, $d \approx 0.5$ nm. The electrostatic energy necessary to hold together one +3 and three −1 chains into a four-tail bundle is then $E_e \approx 3(-1)l_B k_B T/d \approx -9\ k_BT$, in agreement with the estimates from atomistic MD simulations of about $-2.8\ k_BT$ (30%) or about $-2.4\ k_BT$ (95%) per NH_3^+-COO^- ion pair for their cohesive energy (cf. Supporting Information), which is the effective interaction between them mediated by the water environment. Adding the hydrophobic attraction, which is around $-20\ k_BT$/chain from atomistic MD simulations (cf. Supporting Information) gives $E_b \approx -90\ k_BT$. In contrast to ionically driven assembly of incompatible molecules,[31] the assembly discussed here induces short-range attractions among dissimilar molecules of opposite charge, explaining the stability of the ionic crystalline bilayer up to salt concentration n = 500 mM NaCl. As shown in Figure 5b, a single diffraction peak in the WAXS region shows up in all four curves, indicating that the hydrophobic tails are

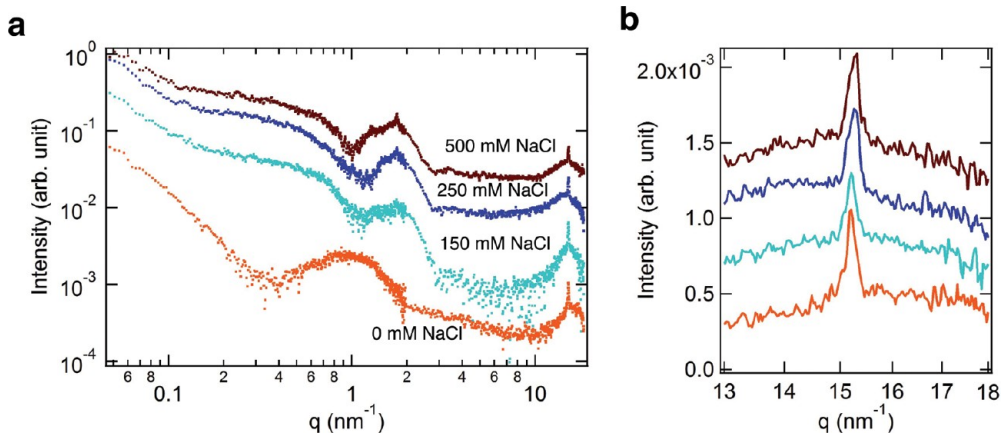

Figure 5. X-ray scattering from bilayers in salt solutions. (a) SAXS−WAXS data showing the scattered intensity *versus* the scattering vector *q* for mixtures of acid C_{15}-COOH and cation C_{16}-K_3 in 0, 150, 250, and 500 mM NaCl solutions (from bottom to top) at pH 4. The three data sets are offset vertically for clarity. The broad oscillations in the SAXS region are consistent with form factors for catanionic bilayers. The small peak at 1.77 nm^{-1} is due to suspended (undissolved) solid palmitic acid. (b) WAXS data for the mixture in 0, 150, 250, and 500 mM NaCl solutions (from bottom to top).

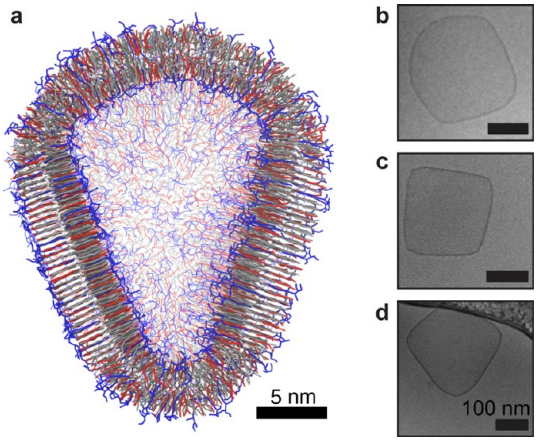

Figure 6. Faceted vesicle observed in simulation and TEM. (a) Representative snapshot of the MARTINI coarse-grained MD simulation where half of the vesicle is omitted for clarity. The ionization degree of the anion is 30%, and the molecules are color-coded as in Figure 3a,b. (b−d) TEM images of low symmetry, highly faceted vesicles observed in the mixture at pH 5.

still crystallized into a hexagonal lattice even at high salt concentrations.

Our results show that though electrostatic interactions can induce the formation of rectangular lattices in membranes of short ionic amphiphiles, the irregular faceted shapes seem to be prominent when the crystalline lattice is hexagonal, which is the ubiquitous symmetry in crystalline shells. To further reveal the morphology at mesoscale level, coarse-grained MD simulations are performed using the MARTINI force field.[32,33] Under MARTINI force field, four heavy atoms are represented by one interaction bead on average (Figure S7 in Supporting Information). Therefore, the atomistic structure is semiquantitatively preserved. In Figure 6a, a MARTINI MD simulation snapshot of the optimal tail packing shows that the internal structure of the vesicle bilayer is not homogeneous. The vesicle surface can be thought as a two-component shell, where one component represents flat crystalline domains while the second component represents the high curvature, liquid-like boundaries between the hard facets. The bilayer packing and thickness in the flat areas are in agreement with the atomistic MD simulations (Figure 3a). Given that the size of the crystalline domains obtained by SAXS is $\sim 30 \times 30$ nm^2, our results suggest that small vesicles (<100−200 nm in diameter), in which only few crystalline domains cover their surfaces, are more likely to be faceted into polyhedral structures with low symmetry (lower than the icosahedra) observed by TEM (Figure 4b−d). On the other hand, large vesicles in which the defects spread over many boundaries have nearly spherical faceted shapes (Figure 1b). The MARTINI MD simulations (Figure 6a) show that the edges of the polyhedra are fluid-like bilayers. We note the possibility that a fluid-like region may exist on the polyhedron only if the packing lattice is hexagonal. This is because the phase diagram for tail packing, as observed in Langmuir films,[28] allows fluid-hexagonal coexistence. In comparison, there does not exist an obvious coexistence region between rectangular-C and fluid phases in monolayers,[28] which may explain why the vesicles are not stable at higher degrees of ionization when the pH is 8 (Figure 1b).

CONCLUSIONS

In conclusion, the pH acts as a switch that controls the crystal structure and therefore the mesoscale morphology of bilayers of coassembled ionic amphiphiles. The low symmetry faceted shapes are due to crystalline domains induced by ionic correlations. These 2D ionic correlations, as in ionic bonding, are not sufficiently screened by the bulk salt, generating membranes that are stable even at high salt concentrations. The ionic non-icosahedra faceted vesicles

are not homogeneous and the facets have a nonzero Young's modulus, akin to crystallized double-tail surfactants[34] or chemically bonded membranes.[35] Their crystalline lattice and morphology, however, are determined by the solution pH. The observed irregular faceted shapes arise only in hexagonal crystalline lattices, where crystalline domains are separated by soft interfaces that bend to release stress. At intermediate pH values, the induced crystalline transition opens the closed membranes. Faceting also arises when strongly charged molecules, such as DNA, are adsorbed into oppositely charged lipid vesicles,[36] which suggests that the geometries found here may also arise in the adsorption of multivalent ions on lipids[37] or cellular membranes.[38] Our results also suggest that spherical-to-faceted reversible transitions can be induced in cationic vesicles by adding (or chelating) metallic multivalent ions,[39] similar to the halophilic archaeon *Haloarcula japonica*, which undergoes a triangular to spherical morphological change after lowering the magnesium concentration in the medium,[40] in addition to other possible kinetic growth mechanisms of faceted geometries.[41] The findings improve our understanding of how molecules self-assemble into robust aggregates with well-defined structures and surface composition stable at physiological ionic conditions and/or high salt concentrations, such as unusual viral capsids,[5] carboxysomes,[8−10] or halophilic organisms.[6,7] We foresee applications of these vesicles to the design and fabrication of functional nanoscale containers. Moreover, our work demonstrates that a local molecular scale change in structure induced by adjusting the solution pH leads to mesoscale structural changes. This process elucidates a mechanism by which chemical energy transforms into mechanical energy, which could be exploited in the design of bioengineered synthetic nanomachines.

MATERIALS AND METHODS

Synthesis. All amino acids and Rink MBHA resin were purchased from Novabiochem Corporation (San Diego, CA). All other reagents and solvents for peptide synthesis were purchased from Aldrich or TCI and used as provided. The synthesis of the *N*-palmitoyl trilysine C_{16}-K_3 was performed using standard manual solid-phase peptide synthesis methods. Briefly, peptides were grown on Rink amide MBHA polystyrene resin, using 4.0 molar equiv of an Fmoc-protected amino acid, 3.95 equiv of 2-(1*H*-benzotriazole-1-yl)-1,1,3,3-tetramethyluronium hexafluorophosphate (HBTU), and 6 equiv of *N*,*N*-diisopropylethylamine (DIEA) for each residue coupled to the resin. The palmitic acid tail was subsequently coupled to the N-terminus of the peptide by adding 8.0 molar equiv of palmitic acid C_{15}-COOH to the peptide in the presence of 7.95 molar equiv of HBTU and 12 molar equiv of DIEA. The palmitic acid was then cleaved from the polystyrene resin, and amino acid side groups were deprotected in 95% trifluoroacetic acid (TFA), 2.5% triisopropylsilane (TIS), and 2.5% deionized water. TFA was removed by rotary evaporation, and the peptide product was collected by precipitation with cold diethyl ether. Peptide C_{16}-K_3 was purified by Varian preparative HPLC using a Waters Atlantis C-18 30 × 250 mm column under a slow elution gradient of 98% to 0% water and acetonitrile (0.1% TFA). Separation with a gradient of 40−60% water over 25 min gave the desired peptide C_{16}-K_3 as the trifluoroacetate salt.

Sample Preparation. Cation C_{16}-K_3 was first dissolved in Milli-Q water at a concentration of 4 mM (typically 750 μL). This solution was added to a centrifuge tube containing 3 equiv of solid palmitic acid C_{15}-COOH. The mixture was agitated and heated to 80 °C for 60 min. Each sample was cooled to room temperature then centrifuged at approximately 2000 rpm for 5 min to remove residual palmitic acid prior to analysis. The pH of this solution was approximately 3 before and after heating. The pH of each sample (except pH 3) was adjusted with 1 M NaOH after heating.

Transmission Electron Microscopy. Cryogenic transmission electron microscopy (cryo-TEM) imaging was performed on a JEOL 1230 microscope, operating at 100 kV. A small droplet of the solution (5−10 μL) was placed on a holey carbon film supported on a TEM copper grid. The grid was held by a tweezer mounted on a Vitrobot VI equipped with a controlled humidity and temperature environment. The specimen was blotted and plunged into a liquid ethane reservoir cooled by liquid nitrogen. The vitrified samples were transferred to a Gatan 626 cryo-holder through a cryo-transfer stage cooled by liquid nitrogen. During observation of the vitrified samples, the cryo-holder temperature was maintained below −180 °C. The images were recorded with a CCD camera.

X-ray Scattering. SAXS and WAXS patterns were collected simultaneously by two separate CCD X-ray areal detectors at the DND 5ID-D undulator beamline of the Advanced Photon Source at Argonne National Laboratory. The sample solution was injected through a capillary tube flow-cell at room temperature to reduce radiation damage. The capillary was surrounded by vacuum to avoid air scattering. Data were collected at an incident photon energy of 10.00 keV (wavelength $\lambda = 1.240$ Å) with the sample to detector distances arranged to allow the 2θ scattering angle range of the SAXS detector to partially overlap the 2θ range covered by the WAXS detector. For purposes of background subtraction, SAXS−WAXS patterns were also collected from the empty capillary and from the capillary containing the solution without the amphiphiles. The exposure time for each image was 10 s, and five images were taken for each sample. The 2D SAXS−WAXS patterns were converted into 1D radial intensity patterns, $I(\theta)$, by circular integration. Sample solutions were prepared as described above.

Theory and Simulations. The effects of correlations on the dissociation of acid and basic groups as a function of the pH value are obtained by Monte Carlo simulations. We model a two-component system on a triangular lattice with two types of sites, those that are acidic (*i.e.*, can be either neutral $q_A = 0$ or negatively charged $q_A = -1$) and those that are basic (*i.e.*, $q_B = 0$ neutral or positively charged $q_B = +1, +2, +3$). The sites are placed on the lattice shown in Figure 3d chosen to approximate the location of acidic and basic headgroups in the experimental system of interest. Three q_B sites are connected to represent a single molecule. The Hamiltonian used in the simulations is given by

$$\frac{H}{k_B T} = \frac{\mu_A}{k_B T}\sum_i Z_i^A + \frac{\mu_B}{k_B T}\sum_i Z_i^B - \frac{1}{2} l_B \kappa \sum_i Z_i^2 + \frac{1}{2}\sum_{i \neq j} Z_i Z_j l_B (-1)^{\eta} \frac{e^{-\kappa r_{ij}}}{r_{ij}}$$

where Z_i is the absolute value of the ionization state of site i (*i.e.*, $Z^A = 0$, 1 and $Z^B = 0$, 1, 2, 3), and $\eta = 0$ (1) if sites i and j have the same (opposite) sign. The chemical potentials are given as

$$\frac{\mu_I}{k_B T} = -\ln 10(\mathrm{pH} - \mathrm{p}K_{a(I)})$$

for I = A, B.

The atomistic MD simulations were performed using the GROMACS package (version 4.5.5). The latest version of the

GROMOS96 54A7 united-atom force field[42] was employed for the amphiphiles; water is modeled using the SPC model. The electrostatic interactions were calculated using the particle mesh Ewald method, and the short-range Lennard-Jones interactions were truncated at 1.2 nm. Two systems representing the ionization degrees of palmitic acid molecules of 30 and 95%, respectively, were investigated, which are correspondingly composed of 660 (30%) and 632 (95%) amphiphiles. The simulations were started from pseudobilayer structures (akin to Figure 4a, no interdigitation), as we care about the equilibrium structure, rather than the slow kinetics of the self-assembling process. The simulation was performed for a duration of 300 ns for the system with 30% ionization of palmitic acid. The formation of the interdigitation in the system with 30% ionization of palmitic acid is very slow, requiring a simulation as long as 1 μs. In the simulations, the area per lipid tail was tracked for the equilibration of the systems.

The MARTINI coarse-grained MD simulation was performed by employing the latest stable MARTINI force field (version 2.1).[32,33] The planar bilayer was prepared and equilibrated at room temperature. Increasing the temperature to 350 K leads to the spontaneous formation of a spherical vesicle. Returning to ambient temperature and removing ~40% of the waters in the vesicle interior sped up the simulation, and faceted vesicles were obtained within 100 ns. The MARTINI MD simulation was performed for the duration of up to 1 μs.

Conflict of Interest: The authors declare no competing financial interest. [#]These authors contributed equally to this work.

Acknowledgment. C.-Y.L., R.S., M.A.G., G.V., M.O.d.l.C., and M.J.B. were funded by DOE-BES DE-FG02-08ER46539. B.F.Q. was funded by DOD NSSEFF award AFOSR (FA9550-10-1-0167), and S.K. was funded by AFOSR (FA9550-11-1-0275). L.C.P., C.J.N., and S.I.S. thank the NSF (DMR-0605427) for financial support. The SAXS/WAXS experiments were performed at the DuPont-Northwestern-Dow Collaborative Access Team (DND-CAT) located at Sector 5 of the Advanced Photon Source (APS) and at Chemical and Materials Science (CMS) located at Sector 12. DND-CAT is supported by E.I. DuPont de Nemours & Co., The Dow Chemical Company, and Northwestern University. Use of the APS, an Office of Science User Facility operated for the U.S. Department of Energy (DOE) Office of Science by Argonne National Laboratory, was supported by the U.S. DOE under Contract No. DE-AC02-06CH11357. This work made use of the Biological Imaging Facility (TEM), Peptide Synthesis Core at IBNAM (HPLC), and the Integrated Molecular Structure Education and Research Center (NMR and MS). The authors thank M. Johnson for the use of the QFDE instrument, S. Weigand and S. Seifert for assistance with the X-ray scattering, M. Seniw for assistance with graphics, and J.-L. Sikorav for useful discussions.

Supporting Information Available: Experimental and simulation methods and results are included. This material is available free of charge *via* the Internet at http://pubs.acs.org.

REFERENCES AND NOTES

1. Spector, A. A.; Yorek, M. A. Membrane Lipid Composition and Cellular Function. *J. Lipid Res.* **1985**, *26*, 1015–1035.
2. Seifert, S. Configurations of Fluid Membranes and Vesicles. *Adv. Phys.* **1997**, *46*, 13–137.
3. Šegota, S.; Teža, D. Spontaneous Formation of Vesicles. *Adv. Colloid Interface Sci.* **2006**, *121*, 51–75.
4. Morigakia, K.; Waldeb, P. Fatty Acid Vesicles. *Curr. Opin. Colloid Interface Sci.* **2007**, *12*, 75–80.
5. Twarock, R. A Tiling Approach to Virus Capsid Assembly Explaining a Structural Puzzle in Virology. *J. Theor. Biol.* **2004**, *226*, 477–482.
6. Walsby, A. E. A Square Bacterium. *Nature* **1980**, *283*, 69–71.
7. Nakamura, S.; Aono, R.; Mizutani, S.; Takashina, T.; Grant, W. D.; Horikoshi, K. The Cell Surface Glycoprotein in *Haloarcula japonica* TR-1. *Biosci. Biotechnol. Biochem.* **1992**, *56*, 996–998.
8. Kerfeld, C. A.; Sawaya, M. R.; Tanaka, S.; Nguyen, C. V.; Phillips, M.; Beeby, M.; Yeates, T. O. Protein Structures Forming the Shell of Primitive Bacterial Organelles. *Science* **2005**, *309*, 936–938.
9. Iancu, C. V.; Morris, D. M.; Dou, Z. C.; Heinhorst, S.; Cannon, G. C.; Jensen, G. J. Organization, Structure, and Assembly of α-Carboxysomes Determined by Electron Cryotomography of Intact Cells. *J. Mol. Biol.* **2010**, *396*, 105–117.
10. Fan, C. G.; Cheng, S. Q.; Liu, Y.; Escobar, C. M.; Crowley, C. S.; Jefferson, R. E.; Yeates, T. O.; Bobik, T. A. Short N-Terminal Sequences Package Proteins into Bacterial Microcompartments. *Proc. Natl. Acad. Sci. U.S.A.* **2010**, *107*, 7509–7514.
11. Vernizzi, G.; Sknepnek, R.; Olvera de la Cruz, M. Platonic and Archimedean Geometries in Multicomponent Elastic Membranes. *Proc. Natl. Acad. Sci. U.S.A.* **2011**, *108*, 4292–4296.
12. Geng, Y.; Dalhaimer, P.; Cai, S.; Tsai, R.; Tewari, M.; Minko, T.; Discher, D. E. Shape Effects of Filaments *versus* Spherical Particles in Flow and Drug Delivery. *Nat. Nanotechnol.* **2007**, *2*, 249–255.
13. Soussan, E.; Cassel, S.; Blanzat, M.; Rico-Lattes, I. Drug Delivery by Soft Matter: Matrix and Vesicular Carriers. *Angew. Chem., Int. Ed.* **2009**, *48*, 274–288.
14. Dias, R. S.; Lindman, B.; Miguel, M. G. DNA Interaction with Catanionic Vesicles. *J. Phys. Chem. B* **2002**, *106*, 12600–12607.
15. Liu, Y.; Hu, C.; Comotti, A.; Ward, M. D. Supramolecular Archimedean Cages Assembled with 72 Hydrogen Bonds. *Science* **2011**, *22*, 436–440.
16. Dubois, M.; Deme, B.; Gulik-Krzywicki, T.; Dedieu, J. C.; Vautrin, C.; Desert, S.; Perez, E.; Zemb, T. Self-Assembly of Regular Hollow Icosahedra in Salt-Free Catanionic Solutions. *Nature* **2001**, *411*, 672–675.
17. Greenfield, M. A.; Palmer, L. C.; Vernizzi, G.; Olvera de la Cruz, M.; Stupp, S. I. Buckled Membranes in Mixed-Valence Ionic Amphiphile Vesicles. *J. Am. Chem. Soc.* **2009**, *131*, 12030–12031.
18. Bressel, K.; Muthig, M.; Prevost, S.; Gummel, J.; Narayanan, T.; Gradzielski, M. Shaping Vesicles-Controlling Size and Stability by Admixture of Amphiphilic Copolymer. *ACS Nano* **2012**, *6*, 5858–5865.
19. Raspaud, E.; Olvera de la Cruz, M.; Sikorav, J. L.; Livolant, F. Precipitation of DNA by Polyamines: A Polyelectrolyte Behavior. *Biophys. J.* **1998**, *74*, 381–393.
20. Wong, G. C. L.; Pollack, L. Electrostatics of Strongly Charged Biological Polymers: Ion-Mediated Interactions and Self-Organization in Nucleic Acids and Proteins. *Annu. Rev. Phys. Chem.* **2010**, *61*, 171–189.
21. Kalsin, A. M.; Fialkowski, M.; Paszewski, M.; Smoukov, S. K.; Bishop, K. J. M.; Grzybowski, B. A. Electrostatic Self-Assembly of Binary Nanoparticle Crystals with a Diamond-like Lattice. *Science* **2006**, *312*, 420–424.
22. Leunissen, M. E.; Christova, C. G.; Hynninen, A. P.; Royall, C. P.; Campbell, A. I.; Imhof, A.; Dijkstra, M.; van Roij, R.; van Blaaderen, A. Ionic Colloidal Crystals of Oppositely Charged Particles. *Nature* **2005**, *437*, 235–240.
23. Salkar, R. A.; Mukesh, D.; Samant, S. D.; Manohar, C. Mechanism of Micelle to Vesicle Transition in Cationic–Anionic Surfactant Mixtures. *Langmuir* **1998**, *14*, 3778–3782.
24. Kaler, E. W.; Herrington, K. L.; Murthy, A. K.; Zasadzinski, J. A. N. Phase Behavior and Structures of Mixtures of Anionic and Cationic Surfactants. *J. Phys. Chem.* **1992**, *96*, 6698–6707.
25. Vernizzi, G.; Olvera de la Cruz, M. Faceting Ionic Shells into Icosahedra *via* Electrostatics. *Proc. Natl. Acad. Sci. U.S.A.* **2007**, *104*, 18382–18386.
26. Hartgerink, J. D.; Beniash, E.; Stupp, S. I. Self-Assembly and Mineralization of Peptide-Amphiphile Nanofibers. *Science* **2001**, *294*, 1684–1688.
27. Svergun, D. I.; Koch, M. H. J. Small-Angle Scattering Studies of Biological Macromolecules In Solution. *Rep. Prog. Phys.* **2003**, *66*, 1735–1782.
28. Kaganer, V. M.; Möhwald, H.; Dutta, P. Structure and Phase Transitions in Langmuir Monolayers. *Rev. Mod. Phys.* **1999**, *71*, 779–819.
29. Tagliazucchi, M.; Olvera de la Cruz, M.; Szleifer, I. Self-Organization of Grafted Polyelectrolyte Layers *via* the Coupling of Chemical Equilibrium and Physical Interactions. *Proc. Natl. Acad. Sci. U.S.A.* **2010**, *107*, 5300–5305.

30. Netz, R. R. Charge Regulation of Weak Polyelectrolytes at Low- and High-Dielectric-Constant Substrates. *J. Phys.: Condens. Matter* **2003**, *15*, S239–S244.
31. Solis, F. J.; Stupp, S. I.; Olvera de la Cruz, M. Charge Induced Pattern Formation on Surfaces: Segregation in Cylindrical Micelles of Cationic−Anionic Peptide-Amphiphiles. *J. Chem. Phys.* **2005**, *122*, 054905.
32. Monticelli, L.; Kandasamy, S. K.; Periole, X.; Larson, R. G.; Tieleman, D. P.; Marrink, S. J. The MARTINI Coarse Grained Force Field: Extension to Proteins. *J. Chem. Theory Comput.* **2008**, *4*, 819–834.
33. Marrink, S. J.; de Vries, A. H.; Mark, A. E. Coarse Grained Model for Semiquantitative Lipid Simulations. *J. Phys. Chem. B* **2004**, *108*, 750–760.
34. Blaurock, A. E.; Gamble, R. C. Small Phosphatidylcholine Vesicles Appear To Be Faceted below the Thermal Phase Transition. *J. Membr. Biol.* **1979**, *50*, 187–204.
35. Percec, V.; Wilson, D. A.; Leowanawat, P.; Wilson, C. J.; Hughes, A. D.; Kaucher, M. S.; Hammer, D. A.; Levine, D. H.; Kim, A. J.; Bates, F. S.; *et al.* Self-Assembly of Janus Dendrimers into Uniform Dendrimersomes and Other Complex Architectures. *Science* **2010**, *328*, 1009–1014.
36. Raspaud, E.; Pitard, B.; Durand, D.; Aguerre-Chariol, O.; Pelta, J.; Byk, G.; Scherman, D.; Livolant, F. Polymorphism of DNA/Multi-Cationic Lipid Complexes Driven by Temperature and Salts. *J. Phys. Chem. B* **2001**, *105*, 5291–5297.
37. Nadler, M.; Steiner, A.; Dvir, T.; Szekely, O.; Szekely, P.; Ginsburg, A.; Asor, R.; Resh, R.; Tamburu, C.; Peres, M.; *et al.* Following the Structural Changes during Zinc-Induced Crystallization of Charged Membranes Using Time-Resolved Solution X-ray Scattering. *Soft Matter* **2011**, *7*, 1512–1523.
38. Christian, D. A.; Tian, A. W.; Ellenbroek, W. G.; Levental, I.; Rajagopal, K.; Janmey, P. A.; Liu, A. J.; Baumgart, T.; Discher, D. E. Spotted Vesicles, Striped Micelles and Janus Assemblies Induced by Ligand Binding. *Nat. Mater.* **2009**, *8*, 843–849.
39. Travesset, A.; Vaknin, D. Bjerrum Pairing Correlations at Charged Interfaces. *Europhys. Lett.* **2006**, *74*, 181–187.
40. Horikoshi, K.; Aono, R.; Nakamura, S. The Triangular Halophilic Archaebacterium *Haloarcula japonica* Strain TR-1. *Experientia* **1993**, *49*, 497–502.
41. Leng, L.; Egelhaaf, S. U.; Cates, M. E. Kinetics of the Micelle-to-Vesicle Transition: Aqueous Lecithin-Bile Salt Mixtures. *Biophys. J.* **2003**, *85*, 1624–1646.
42. Schmid, N.; Eichenberger, A. P.; Choutko, A.; Riniker, S.; Winger, M.; Mark, A. E.; van Gunsteren, W. F. Definition and Testing of the GROMOS Force-Field Versions 54A7 and 54B7. *Eur. Biophys. J.* **2011**, *40*, 843–856.